ORIGINAL ARTICLE

A real-time ZTD model in China using ERA5 and GNSS based on empirical orthogonal function method

Yu Wang[1,2] · Shuanggen Jin[1,3] · Cheng Liu[4] · Guanjun Zhang[4] · Yunlong Zhang[4]

Abstract

Zenith total delay (ZTD) is a significant error source in Global Navigation Satellite System (GNSS) operations. While empirical ZTD models are widely used, the accuracy of these models is relatively low. In contrast, real-time models typically rely on interpolation methods and encounter challenges when sparse GNSS stations are operating. In this paper, we present a new ZTD model based on empirical orthogonal function (EOF) methodology. Initially, ZTD derived from hourly ERA5 data, is subjected to decomposition into two distinct components: spatial and temporal. Subsequently, an artificial neural network (ANN) model is employed to train the GNSS-derived ZTD data obtained from the Crustal Movement Observation Network of China (CMONOC) to predict the temporal component. The real-time gridded model is then constructed by multiplying the predicted temporal component with the spatial component. This EOF-based ZTD model (referred to as EOFM) is evaluated by GNSS-derived ZTD, ERA5-derived ZTD, and radiosonde-derived ZTD data for the year 2022. The results show that EOFM has a mean bias of 0.02 cm and -0.18 cm for internal and external validation, along with a mean root mean square (RMS) of 1.74 cm and 1.89 cm for internal and external validation. Furthermore, the RMS values for EOFM are 1.70 cm and 2.49 cm when compared to ERA5-derived ZTD and radiosonde-derived ZTD, respectively. Remarkably, this innovative model can provide real-time ZTD estimates for the region with limited or no coverage by GNSS stations, even when GNSS stations are not present in the area with achieving an impressive RMS of 1.55 cm.

Keywords GNSS · Tropospheric delay · EOF · ERA5

Introduction

GNSS technology has extended its applications in diverse fields, such as hydrogeodesy (White et al. 2022), meteorology (Wang and Jin 2023; Jin et al. 2011), agriculture (Guo et al. 2018) and remote sensing (Jin et al. 2024). GNSS precise point positioning (PPP) can achieve absolute positioning with centimeter-level accuracy. Real-time PPP is now garnering increased attention for applications like early warning of earthquakes (Jin et al. 2022) and tsunamis (Tsushima et al. 2014), as well as its potential in self-driving cars and drones (Li et al. 2021b). However, ZTD is a significant source of error in GNSS positioning (e.g. Jin et al. 2010, 2011a), affecting both positioning accuracy and convergence time, particularly in the elevation direction (Ding 2020; Li et al. 2021a; Lu et al. 2023).

ZTD can be broadly categorized into zenith hydrostatic delay (ZHD) and zenith wet delay (ZWD). While ZHD can be relatively easily modeled using the Saastamoinen model (Saastamoinen 1972), the accurate modeling of ZWD remains a formidable challenge due to the significant spatial and temporal variability of water vapor content in the atmosphere. Therefore, the modeling of tropospheric wet delay has emerged as a limiting factor in space geodetic observations. Several studies (de Oliveira et al. 2017; Lu et al. 2017) have demonstrated that providing accurate priori values for

✉ Shuanggen Jin
  sgjin@shao.ac.cn

1 Shanghai Astronomical Observatory, Chinese Academy of Sciences, 80 Nandan Road, Shanghai 200030, China

2 School of Astronomy and Space Science, University of Chinese Academy of Sciences, Beijing 100049, China

3 School of Surveying and Land Information Engineering, Henan Polytechnic University, Jiaozuo 454003, China

4 Academy of Geomatics and Geographic Information, China Railway Design Corporation, Tianjin 300308, China

wet delays can significantly enhance the performance of precise kinematic positioning, leading to improvements in both convergence time and positioning precision. Empirical tropospheric models, like UNB3 (Mendes and Langley 1999; Leandro et al. 2006), TropGrid (Krueger et al. 2005; Schüler 2014), GEOFT (Sun et al. 2017), IGGtrop (Li et al. 2012, 2015), and GPT series (Boehm et al. 2007; Lagler et al. 2013; Böhm et al. 2015; Landskron and Böhm 2018), are favored in real-time navigation tasks because of their self-sufficiency. These models do not rely on external data as input, allowing them to directly provide ZTD values based on the day of the year. These self-contained models employ harmonic functions to capture the periodicity of historical meteorological parameters obtained from radiosondes and reanalysis data. Among the models mentioned above, the widely recognized GPT series has gained the most widespread adoption. It demonstrates a global accuracy of 4 cm at $1° × 1°$ spatial resolution (Xu et al. 2023). However, these empirical models often introduce biases of several centimeters (Yao et al. 2015) and are unable to account for short-term fluctuations in tropospheric delay (Zhang et al. 2018), especially during severe weather conditions. To address this challenge, some studies have explored the combination of numerical weather prediction (NWP) data with empirical models. For instance, Lu et al. (2016) utilized forecasts from ECMWF to generate ZTD parameters, effectively reducing convergence times. In a similar vein, Lu et al. (2017) incorporated tropospheric delay parameters derived from global forecast system (GFS) into BeiDou real-time PPP, yielding positive outcomes in terms of shorter convergence times. Meanwhile, Zhang et al. (2022) utilized GNSS-derived ZTD to refine the GFS forecasts, and this approach has been successfully implemented in BeiDou PPP services. These models have the capacity to forecast tropospheric delays on a global scale. However, the temporal and spatial resolution of the ZTD derived from NWP data depends on the NWP itself. As the resolution increases, the demand for computational resources and integration time increases exponentially. Additionally, the forecasting accuracy of NWP data tends to deteriorate over time.

In such situations, it becomes more appropriate to construct high-precision tropospheric models based on real-time or near real-time GNSS measurements. Zhang et al. (2018) proposed a gridded tropospheric mode that can be applied globally depending on the spread of a GNSS network. This model combines the GNSS network with empirical IGGtrop models. Lou et al. (2018) used ERA-Interim data to establish an inverse scale height model and integrated it with the GNSS network to create a gridded model. Similar research has been undertaken by Xia et al. (2023), who constructed a gridded model of elevation normalization factors using ERA5 reanalysis data to enhance the accuracy of real-time

ZTD over extensive height regions. However, it is worth noting that all these models rely on interpolation methods, and their resolutions are constrained by the distribution of GNSS stations. In regions with limited station coverage, such as the Tibetan Plateau in China, the accuracy is comparatively lower than in areas with more stations. Hence, there is a clear benefit in developing a method that utilizes real-time GNSS data to produce accurate results in regions with either limited or no monitoring stations.

In this study, we developed a new ZTD model based on empirical orthogonal function (EOF). This approach involves integrating ERA5 reanalysis data with the GNSS station network. By utilizing the ZTD data from the CMONOC network from 2012 to 2021, we employed ANN to model the principal components (PCs) obtained through the EOF method. Consequently, we construct a real-time $0.25° × 0.25°$ gridded ZTD model over China. GNSS data and radiosonde data collected in 2022 are used to assess the accuracy of this new model. In the following section, we elaborate on the data and methods employed. Subsequently, we outline the specific steps to establish the model and validate it by comparing with ZTD values derived from ERA5, GNSS, and radiosonde data. Additionally, we emphasize the advantages and discuss future prospects in the subsequent section, and finally conclusions are given.

Data and methods

This section provides an overview of the data and methods utilized in this study. The primary sources of ZTD are derived from GNSS and meteorological variables. The intricate process involved in our EOF-based approach is then meticulously described.

ZTD from GNSS

CMONOC is an extensive network designed to monitor a wide range of geophysical parameters in China. This network is dedicated to observing crustal movement, changes in the gravitational field, fluctuations in water vapor content in the atmosphere, and variations in ion density and distribution in the ionosphere. CMONOC distribution extends across the entire expanse of China, and its design ensures both high spatial and temporal accuracy. In this study, data from 234 stations are obtained from Shanghai Global Navigation Satellite System Analysis Center. The SHA GNSS analysis center adheres to IGS data analysis strategies, employing a zero-difference approach with 5-minute sampling data from a carefully selected global GNSS network (Chen et al. 2012, 2014). The ZTD in this study is calculated using GAMIT/GLOBK software at a 1-h resolution to

match the temporal resolution of ERA5. Figure 1 illustrates the distribution of these stations, along with their respective altitudes. When GNSS stations are selected for establishing the model, our objective is to ensure a relatively even distribution of training points. This approach facilitates an accurate characterization of the patterns in ZTD distributions. Additionally, it is imperative that the stations possess a sufficient quantity of data for training purposes. Consequently, stations located in Tibet are excluded from the model due to an insufficient volume of data.

ZTD from meteorological data

ERA5 is the fifth-generation ECMWF atmospheric reanalysis product, which provides hourly estimates of a large number of atmospheric, land and oceanic climate variables (Hersbach et al. 2023). In this study, the meteorological variables of temperature, absolute humidity, and geopotential height are utilized in the computation of ZTD. These variables are available at a horizontal resolution of 0.25°×0.25° and encompass 37 vertical layers. Additionally, radiosonde measurements offer vertical profiles of meteorological variables, such as temperature, humidity, and pressure, at different altitudes. In this study, we employed data from 38 sounding stations that are evenly distributed in mainland China (Fig. 1), to validate our model. These sounding measurements are conducted twice daily, at UTC 00:00 and 12:00.

When using meteorological data to obtain ZTD, it can be divided into two components:

$$ZTD = ZHD + ZWD \qquad (1)$$
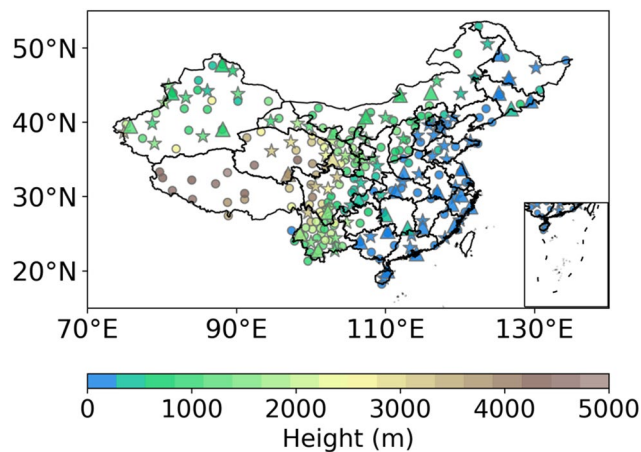
where ZHD denotes zenith hydrostatic delay and ZWD denotes zenith wet delay. ZHD can be calculated using the Saastamoinen (1972) formula:

$$ZHD = \frac{0.0022768\,p}{1 - 0.00266\cos(2\varphi) - 0.00028h} \qquad (2)$$

where p denotes the pressure in hPa, ϕ denotes the latitude in radian, h denotes the height in kilometer. As for ZWD, it can be calculated by Bevis et al. (1992):

$$ZWD = 10^{-6} \int \left((k_2 - k_1 \frac{R_d}{R_v})\frac{p_w}{T} + k_3 \frac{p_w}{T^2} \right) dz \qquad (3)$$

where $k_1 = 0.776 KPa^{-1}$, $k_2 = 0.704 KPa^{-1}$, $k_3 = 373 K^2 Pa^{-1}$ are refractivity constants, $R_d = 287(kmol\ K)^{-1}$ and $R_v = 471(kmol\ K)^{-1}$ are gas constant for dry air and water vapor, p_w denotes the partial pressure of water vapor in pascal, and T denotes temperature in kelvin.

When dealing with gridded ZTD, we standardize the ZTD values to a consistent height using an exponential function. This normalization process helps mitigate the influence of varying elevations, and it is achieved as follows:

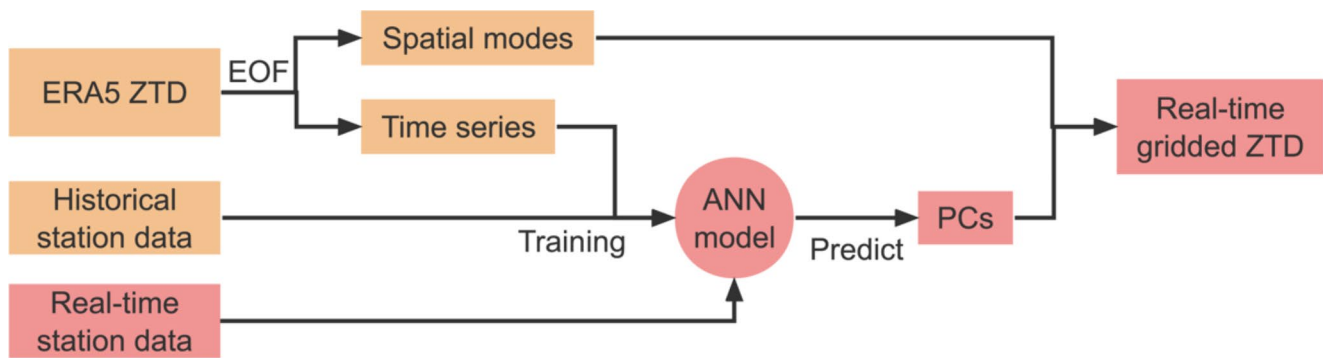$$ZTD = ZTD_0 \times e^{-\beta \frac{1}{h_0}} \qquad (4)$$

where ZTD_0 denotes the zenith tropospheric delay at the bottom layer of the meteorological data at h_0. Therefore, the zenith tropospheric delay at a specific station at a height of h_s can be expressed as follows:

$$ZTD_S = ZTD \times e^{-\beta\,h_s} \qquad (5)$$

where β is an exponential decay constant that varies with latitude, and can be referred to in Chen et al. (2019).

EOF-based approach for ZTD modeling

Our EOF-based model is designed to produce real-time gridded ZTD data by integrating historical reanalysis data and ZTD observations from multiple GNSS stations. This method involves decomposing the three-dimensional historical ZTD variable, which is a function of time, latitude, and longitude, into two separate components: the spatial pattern of ZTD and the temporal series of ZTD. By having the spatial pattern of ZTD, we can create gridded ZTD data as long as we possess the temporal component. Figure 2 illustrates the workflow of this model. First, we decompose the historical ZTD data from ERA5, which covers the years 2012 to 2021. Next, we employ ZTD observations from the CMONOC network to train an ANN model that captures

Fig. 1 Distribution and height of CMONOC and sounding stations. Stars denote the CMONOC stations that are used for real-time ZTD modeling, circles denote the CMONOC stations that are used for external validation, and rectangles denote the radiosound stations

Fig. 2 Workflow of the established real-time EOF-based model. The orange blocks indicate the training part, and the red blocks indicate the predicting part

the principal components. Once the model is trained, it can be used for years. In real-time situations, ZTD measurements from CMONOC serve as inputs to the ANN model. The model then generates gridded ZTD data at the same frequency as the input, such as every 5 min or every hour, by incorporating spatial patterns. Users can retrieve ZTD data based on specific latitude, longitude, and time.

EOF analysis is a commonly used analytical methodology for analyzing the temporal and spatial characteristics of various variables. Numerous studies have applied this approach to scrutinize the global and regional spatiotemporal patterns and fluctuations in various parameters, such as temperature (Kessler 2001), water vapor (Xu et al. 2022), crustal deformation (Neha and Pasari 2022), and total electron content (Li et al. 2019). Detailed information on the computational steps involved in the EOF analysis can be found in Monahan et al. (2009). After the computation of the EOF, the resultant equation is as follows:

$$X = EOF \times PC \qquad (6)$$

where X denotes the raw variable, EOF denotes the spatial functions, PC refers to the principal components. Typically, the EOF represents the variation pattern of the ZTD, and PC indicates the amplitude of the corresponding pattern. Consequently, the product of these two quantities encapsulates the variation in ZTD.

ANN is a network composed of numerous neurons, typically organized into three fundamental layers: the input layer, hidden layer, and output layer (Hinton 1989). Neurons within each hidden layer sum the inputs from various neurons in the preceding layer, applying different weights, and then transmitting this sum to the next layer under the action of a certain threshold and activation function. The output layer computes its result through the weighted linear summation of the final hidden layer's output. The primary advantage of ANNs lies in their ability to train nonlinear models with superior results, yielding outcomes that often

surpass those achievable with linear models. This distinct attribute makes ANNs a valuable tool for complex problem-solving, as they can effectively capture and represent intricate patterns and associations within the data. In this study, the artificial neural network model utilizes backpropagation for training and the adaptive moment estimation (Adam) algorithm to update parameters. To facilitate training and evaluation, the time series data from 2012 to 2021 is subject to a random partition, segmenting it into training and validation sets. Specifically, 80% of the data is allocated to the training set, while the remaining 20% is reserved for the validation set. The inputs to the ANN model consist of GNSS-derived ZTD values from 64 stations at a single time point. These stations are selected with long time available data and relatively even distribution across the China. The model's hidden layers comprise three layers with 128, 32, and 8 neurons, respectively. The model's output predicts the PC at that specific time.

Results and validation

In this section, we begin by outlining the detailed steps taken to establish our model. This includes the estimation of ERA5-derived ZTD, the application of EOF analysis for ZTD, and an exploration of the upper limits of this method. Subsequently, we assess the accuracy of our model by comparing it with ERA5-derived ZTD, GNSS-derived ZTD from CMONOC, and radiosonde-derived ZTD. Furthermore, we delve into the evaluation of accuracy across different seasons and heights to gauge the effectiveness of our model.

Development of EOFM

We initially assess the accuracy of ERA5-derived ZTD prior to the application of the EOFM process. This preliminary assessment is crucial as it sets a theoretical upper

limit on the final accuracy achievable through EOFM. In Fig. 3, we present the bias and RMS comparisons between ERA5-derived ZTD and CMONOC ZTD data from 2012 to 2021. The absolute bias values consistently exhibit a limited range, primarily remaining within a scope of 1 centimeters or less. However, we observe relatively large bias values in southern China, where there is more water vapor in the air, leading to significant changes of ZTD. Similar observations are evident in the RMS analysis, where ERA5-derived ZTD in southern China shows elevated RMS values. The mean bias and RMS values for all stations are -0.02 cm and 1.25 cm, respectively, which aligns closely with the outcomes reported by Zhang et al. (2022).

We choose the first twenty modes of ERA5-derived ZTD according to the North test, which collectively account for more than 95% of ZTD variations. We will use these modes for the subsequent steps in the EOFM process. Each mode represents distinct spatial characteristics of ZTD variation, some of which can be explained mechanistically. As an exemplification, Fig. 4 illustrates the spatial patterns for the first four EOF modes of ERA5-derived ZTD and their corresponding temporal series. Specifically, the first mode
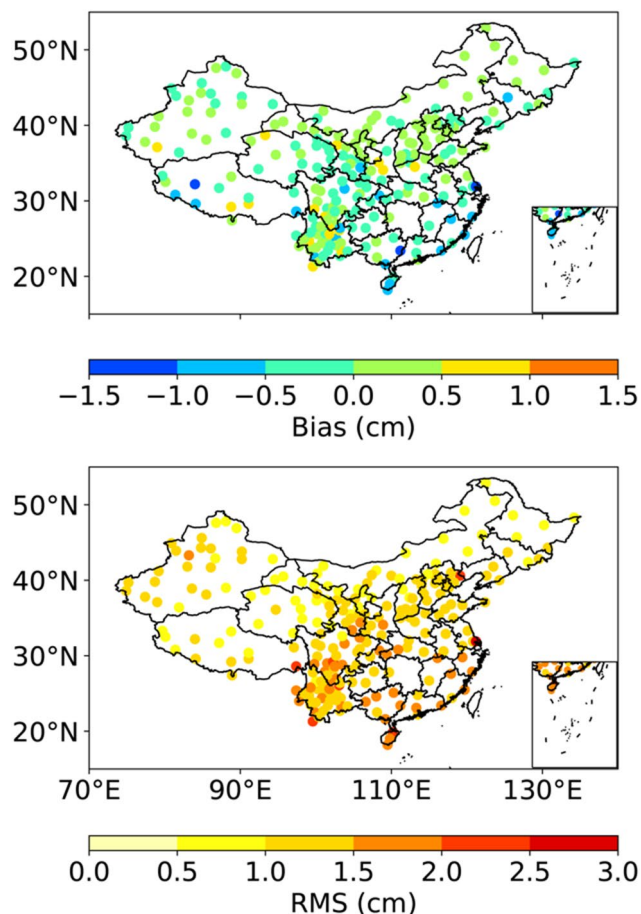
**Fig. 3** Bias (top) and RMS (bottom) between ERA5-derived ZTD and CMONOC ZTD

demonstrates the annual variation of ZTD in China, influenced by annual changes in temperature, pressure, and water vapor content. The second and third modes exhibit north-south and west-east variations, attributable to differences in water vapor content driven by the monsoon. Unlike the first mode, the second PC displays short-term variations layered over seasonal cycles. In contrast, the third PC lacks clear seasonal cycles but exhibits seasonal amplitude variations. Moving on to the fourth mode, it reveals a variation centered in Central China, and its PCs exhibit distinct seasonal amplitude cycles. To enhance our comprehension of the temporal characteristics exhibited in these time series, we conducted a wavelet analysis in Fig. 5. For the first PC, a discernible annual variation emerges as the primary harmonic component. Supplementary periodicities, such as those occurring on a fortnightly scale, are discernible, albeit with relatively diminished power in comparison to the dominant annual cycle. In the case of PC2, pronounced variations manifest at a seasonal scale, accompanied by significant oscillations at a ten-day periodicity, which aligns with the cyclic patterns of weather systems prevalent in Eastern Asia. Moreover, a notable high-frequency daily oscillation is observed, which plausibly reflects the diurnal fluctuations in temperature and atmospheric pressure. PC3 and PC4, which are associated with smaller-scale characteristics, prominently exhibit ten-day oscillations as their prevailing harmonic components, with the intensity of these oscillations displaying an annual variation.

Figure 6 shows RMS between the reconstructed ZTD and its original ERA5-derived ZTD. This reconstruction uses the actual spatial patterns and PCs. Consequently, this RMS represents an additional upper performance for EOFM. Across the majority of regions, the RMS values are less than 1.5 cm. While in western China, they are predominantly below 1 cm owing to the low water vapor content and high altitudes.

Validation of EOFM

The validation of EOFM is primarily divided into two key components in this study. First, it involves a comparison with ERA5-derived ZTD to assess the effectiveness of the EOF-based method. Second, it entails a comparison with GNSS-derived ZTD and radiosonde-derived ZTD to evaluate its real-time accuracy. The GNSS station network in this study exhibits a dense distribution throughout China, enabling a comprehensive assessment of accuracy across the entire China.

Figure 7 depicts the bias and RMS differences between ZTD derived from EOFM and ERA5, alongside ZTD from the VMF3 product. The VMF3 product provides real-time troposphere delay data at a resolution of $1° \times 1°$, with an
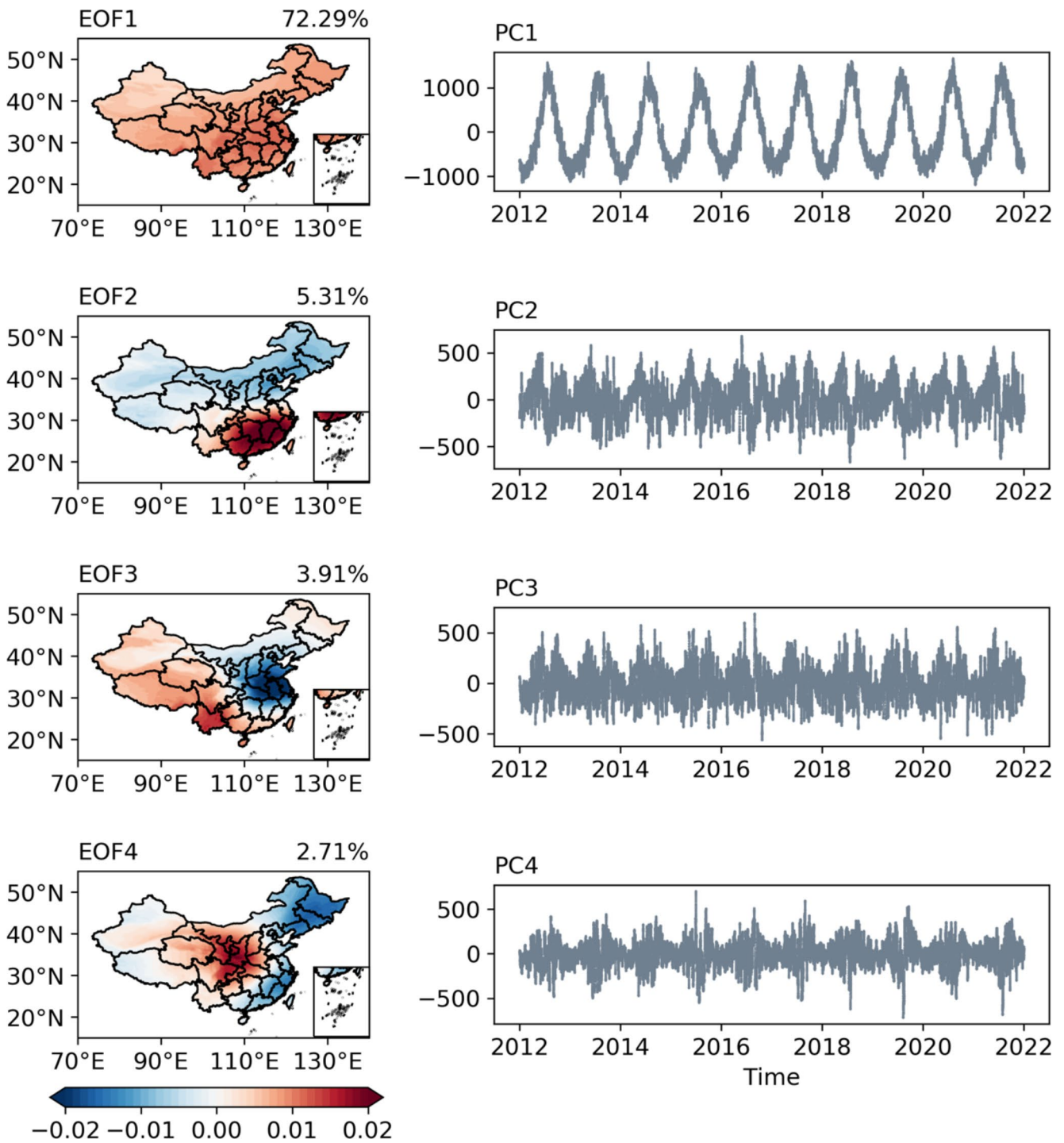
Fig. 4 The spatial patterns (left) and temporal series (right) for the first four EOF modes of ERA5-derived ZTD from 2012 to 2021 in China

overall accuracy of about 1.5 cm in China (Yang et al. 2021). It has been widely used for comparing the performance of various real-time ZTD models. The comparison between ZTD derived from EOFM and ERA5 is divided into three sections: training results, validation results using 80% and 20% of data from 2012 to 2021, and independent test results in 2022. The distributions of bias and RMS

values in both the training and validation datasets exhibit a notable similarity, characterized by mean values of -0.10 cm and 1.34 cm for both the training and validation set. This implies the effective training of the ANN model. In 2022, bias exhibits a distinct west-east distribution, with positive values observed in western China and negative values in eastern China. The RMS demonstrates a distribution similar
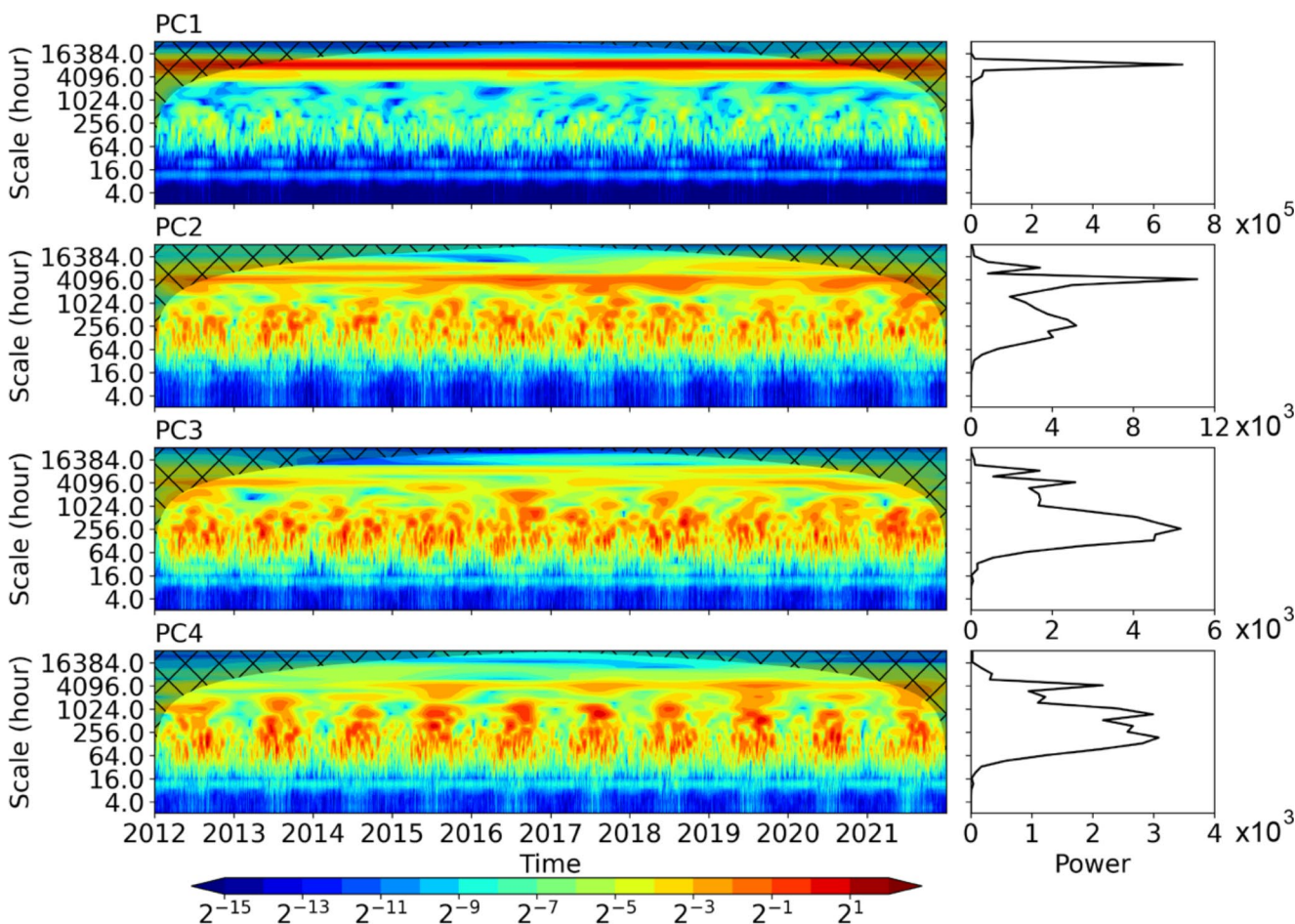
Fig. 5 Wavelet analysis on the time series of the first four PCs. The left panel displays the wavelet spectrum power for each respective PC, with cone areas indicating the influenced regions. The right panel presents the averaged wavelet spectrum
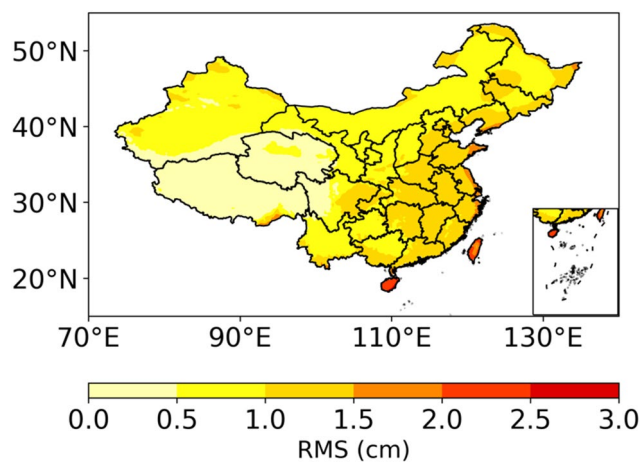

Fig. 6 RMS between the reconstructed EOF-based ZTD and the ERA5-derived ZTD

to that seen in training and validation results, albeit with larger values of 1.70 cm. In 2022, China experienced the emergence of an abnormal heat wave, which may have been further compounded by the ongoing changes in climate

(Zhang et al. 2023). Consequently, the increased deviations in 2022, in comparison to the training and validation results, can be attributed to the fact that the EOF analysis was conducted from 2012 to 2021. The results from VMF3 are quite complex. The mean bias between VMF3 and ERA5-derived ZTD is 0.23 cm, with significant positive biases observed in southeast China. In contrast, negative biases are mainly present in northeast China and parts of Xinjiang Province. The distribution of RMS values is similar to that of EOFM, with large RMS values exceeding 2 cm predominantly in southeast China, while other regions have relatively smaller RMS values. However, VMF3 products show large RMS values in some areas of Xinjiang Province. Overall, VMF3 products have a mean RMS value of 1.84 cm in China.

A more effective comparative analysis of model performance against CMONOC ZTD is provided in Fig. 8. Both the validation and test results closely approximate the training results. An intriguing observation emerges when considering VMF3 ZTD products, which exhibits a noteworthy positive bias within the Xinjiang Province and central China. Regarding the RMS values, they exhibit favorable
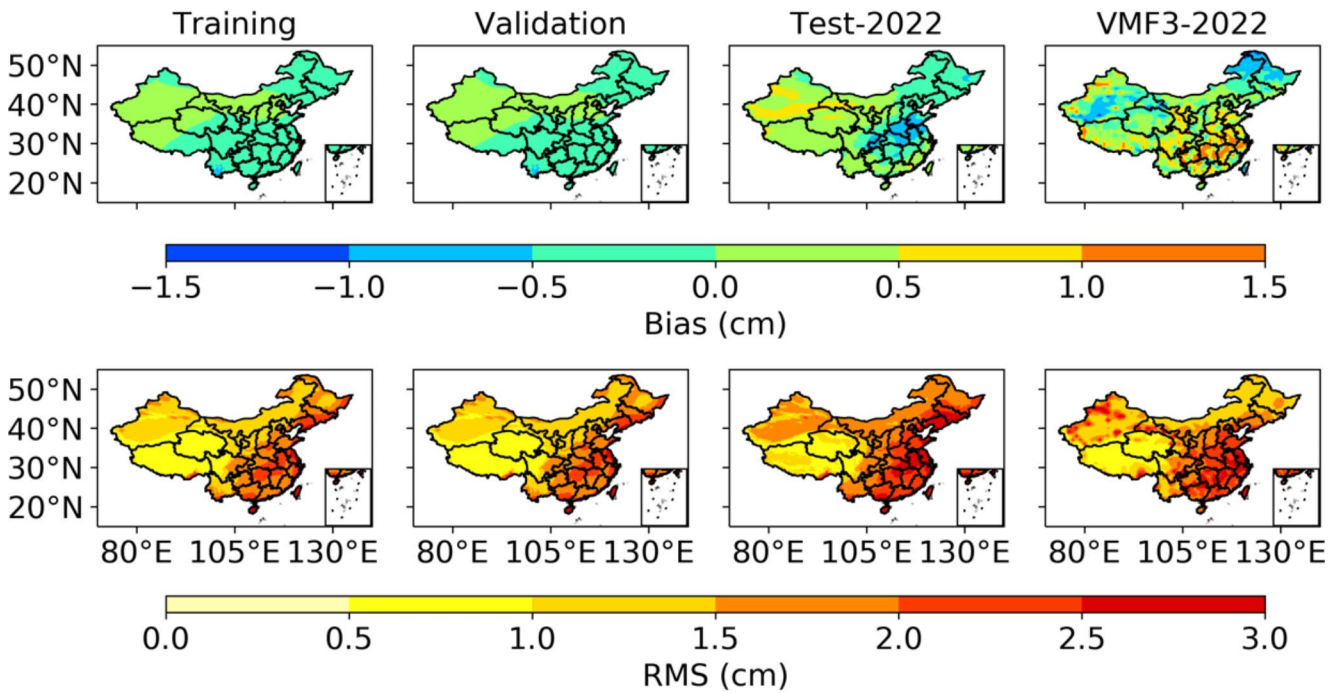
Fig. 7 Bias (top) and RMS (bottom) between the model-derived ZTD and ERA5-derived ZTD. The first and second columns show the training and validation results from 2012 to 2021. The third and last columns show the test results for EOFM and VMF3 in 2022
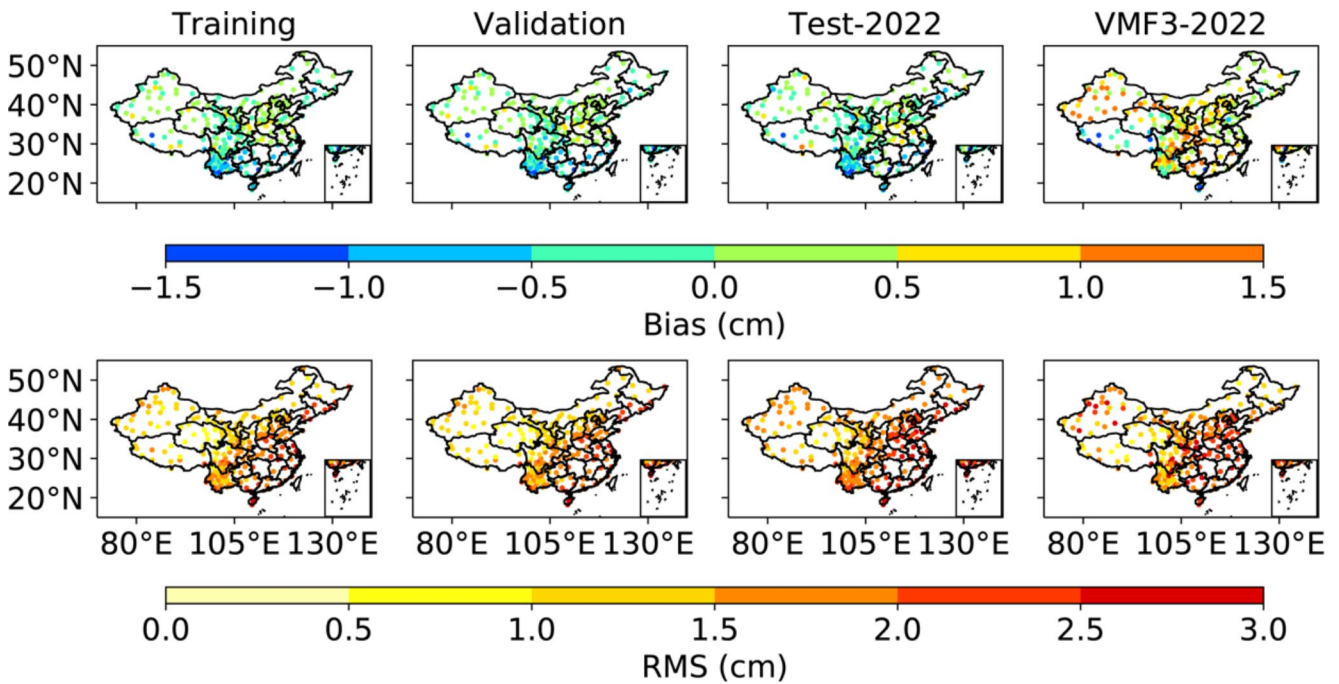
**Fig. 8** Same as in Fig. 7, but compared to CMONOC ZTD

characteristics in the majority of stations, with the exception of a few outliers. The RMS values for the training and validation datasets are both 1.55 cm. These findings underscore the efficacy of the ANN model's training. Moreover, RMS values consistently register below 1.5 cm within Tibetan regions, which can be attributed to their higher altitudes. The

RMS distribution aligns itself with the patterns observed in the training and validation sets. Specifically, Tibetan regions exhibit smaller RMS values, while eastern China displays larger RMS values. However, the 2022 test results manifest a discernible divergence, with RMS values being approximately 0.3 cm larger than those of the preceding

Table 1 Bias and RMS statistics of EOFM ZTD compared to CMONOC ZTD (unit: cm)

|		Mean	Min	Max
Inner-accuracy	Bias	0.02	-0.73	1.41
	RMS	1.74	1.09	2.53
External-accuracy	Bias	-0.18	-2.37	1.12
	RMS	1.89	0.80	2.95
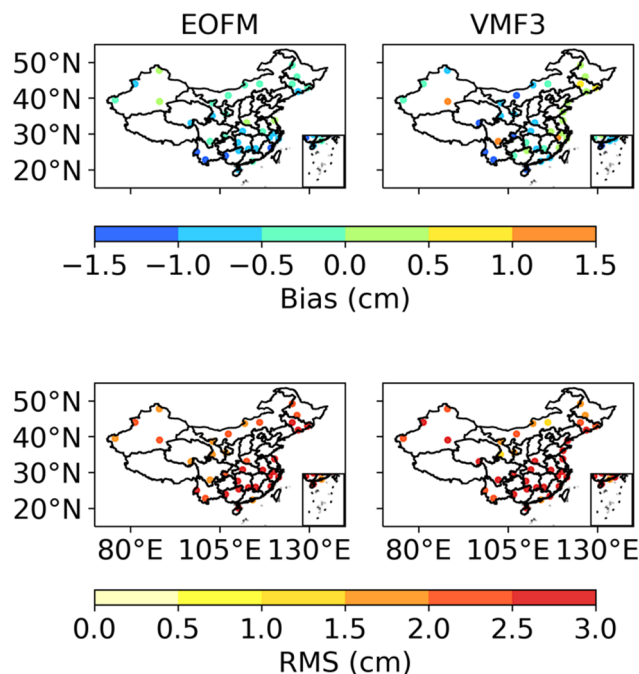
Fig. 9 Bias (top) and RMS (bottom) between the model-derived ZTD and radiosonde-derived ZTD. The first and last columns show the results for EOFM and VMF3, respectively

training and validation sets. The mean RMS value for the 2022 test set is 1.86 cm, whereas the mean RMS value for VMF3 products is slightly lower at 1.84 cm. This EOF-based modeling approach achieves accuracy comparable to NWP-based ZTD products but requires significantly fewer computing resources. Furthermore, Table 1 presents an assessment of both internal and external accuracy, measuring the precision of stations included and excluded from the modeling process. Overall, there are relatively small disparities between internal and external stations, underscoring the uniformity and consistency of this EOF-based modeling approach. However, external stations show a wider range of values due to their greater number. Although this external precision of EOFM is slightly less favorable when compared to CMONOC, it aligns with the accuracy levels of the high-precision real-time ZTD model of China reported in Xia et al. (2023).

Furthermore, we compared the model results with radiosonde-derived ZTD from 48 radiosonde stations across China in 2022 (Fig. 9). There is a systematic bias between the models' ZTD and the radiosonde-derived ZTD. The EOFM model generally shows negative biases across most regions, while the VMF3 product displays significant positive biases in the eastern regions and a broader distribution of negative biases in central China. Both models exhibit relatively high RMS errors, particularly in southern China, with the VMF3 model showing slightly higher RMS values in western China. The mean RMS for EOFM model and VMF3 product are 2.49 cm and 2.54 cm, respectively.

Additionally, we conducted evaluations across diverse seasons (Fig. 10) and elevations (Fig. 11). The VMF3 product demonstrates a relatively consistent bias in estimating ZTD across different seasons. Specifically, VMF3 tends to underestimate ZTD in the Tibetan region, while it exhibits an overestimation bias in both Xinjiang Province and the central part of China. This pattern of bias is indicative of a regional dependency in the VMF3's performance, likely influenced by the distinct atmospheric and topographic conditions prevalent in these areas. Conversely, the EOFM exhibits significant variations in its bias depending on both seasonal and regional factors. The bias in EOFM is relatively minimal during the spring and autumn seasons, whereas it becomes more pronounced during the summer and winter months. The bias of EOFM shows a clear geographical trend, increasing gradually from the southeastern to the northwestern parts of China. In the summer, EOFM predominantly underestimates ZTD across most regions of China. In contrast, during the winter, EOFM tends to overestimate ZTD values. In terms of comparative performance, EOFM outperforms VMF3 in the regions of Tibet and Xinjiang. This superiority is evident through the lower RMS values of EOFM in nearly every season, suggesting a more accurate and reliable performance in these areas. The superior performance of EOFM in these specific regions can be attributed to its ability to account for the unique meteorological patterns and geographical characteristics that influence ZTD estimation. We categorized the CMONOC stations into five groups based on altitude: 0–500 m, 500–1000 m, 1000–2000 m, 2000–3000 m, and higher than 3000 m. With the exception of stations situated above 2000 m, the VMF3 product consistently demonstrates a strong positive bias across the other four altitude groups throughout 2022. This positive bias is particularly evident in stations located at altitudes between 500 and 1000 m. The magnitude of this bias is significantly higher during the summer months, while it diminishes during the winter season. Conversely, the EOFM product exhibits minimal bias across all altitude groups over the same period. However, it is noteworthy that during the summer, the EOFM product displays a marked negative bias, particularly pronounced for stations situated at altitudes ranging from 2000 to 3000 m. Regarding the RMS values, the EOFM product exhibits comparable
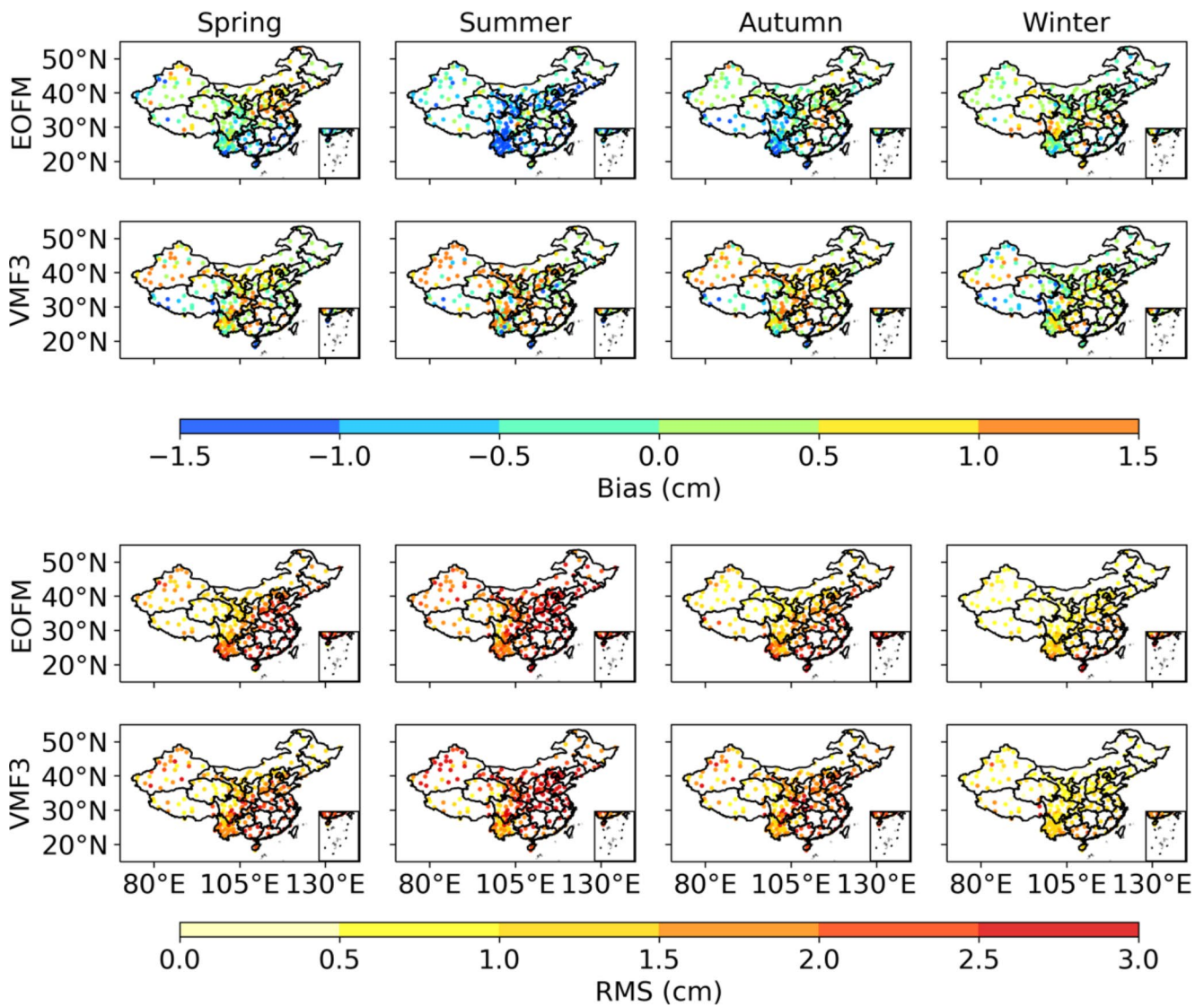
Fig. 10 Bias (top) and RMS (bottom) between the model-derived ZTD and CMONOC ZTD in different seasons. The columns from left to right are the results of spring, summer, autumn, and winter, respec-tively. The first and last rows in each panel are the results for EOFM and VMF3 respectively

values across all altitudes and seasons with those of the VMF3 product. Generally, RMS values show a tendency to decrease with increasing altitude. Nevertheless, during the winter season, RMS values remain relatively consistent across different altitudes. Table 2 provides a comprehensive summary of the characteristic performance of the EOFM product, as illustrated in Fig. 11.

Discussion

Previous real-time ZTD models are mainly relied on inter-polation techniques. However, it is important to note that the utilization of interpolation methods may degrade the preci-sion, as they do not fully account for the physical constraints

associated with the distribution of water vapor in the atmo-sphere. This deficiency becomes particularly pronounced in regions where GNSS stations are sparsely distributed, rendering the interpolation-based approach less robust. The core objective of our study is to introduce a methodology that has not been previously advanced. This innovative approach is designed to furnish real-time ZTD estimates even in areas without or with minimal coverage by GNSS stations.

To further underscore the substantial advantages of our model, we proceed to present a discussion of real-time results obtained in the region of Tibet. Tibet, located in the southwestern border of China, covers an extensive portion of the Tibetan Plateau, with a vast territory spanning 1,228,400 square kilometers. This area constitutes approximately
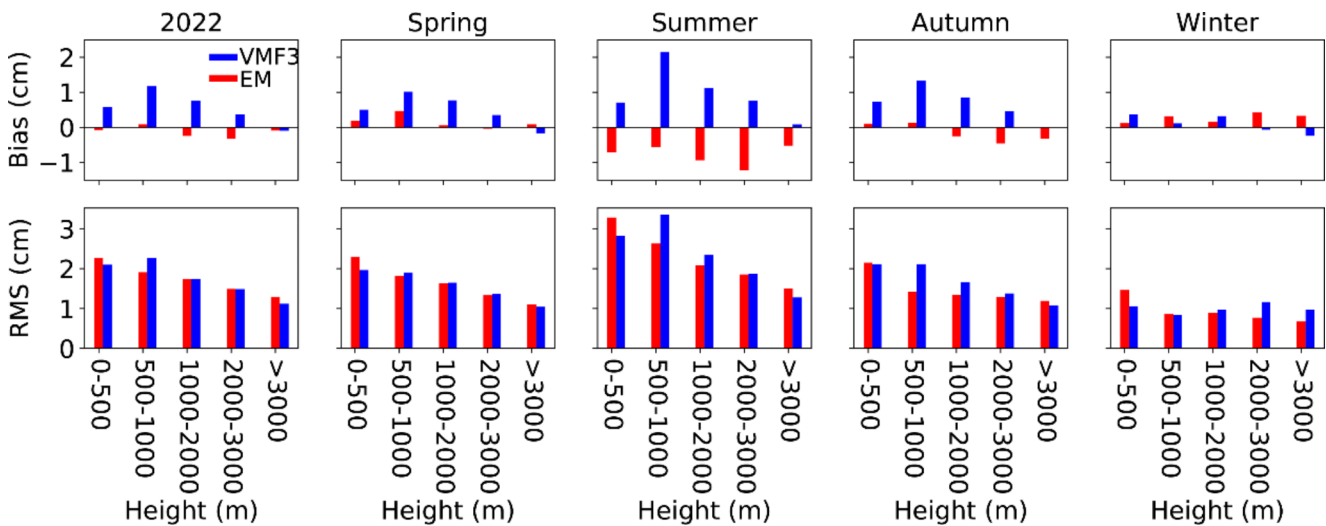
Fig. 11 Bias (top) and RMS (bottom) between the model-derived ZTD and CMONOC ZTD at different heights. The columns from left to right are results for the whole of 2022 and spring, summer, autumn, and winter in 2022, respectively. Red and blue bars indicate EOFM and VMF3 results, respectively

Table 2 Bias and RMS statistics of EOFM ZTD compared in difference seasons and heights (unit: cm)

Height (m)	Spring		Summer		Autumn		Winter		Mean	
	Bias	RMS	Bias	RMS	Bias	RMS	Bias	RMS	Bias	RMS
0-500	0.19	2.30	-0.71	3.28	0.11	2.15	0.12	1.46	-0.07	2.26
500–1000	0.47	1.81	-0.57	2.63	0.13	1.43	0.32	0.86	0.09	1.91
1000–2000	0.06	1.63	-0.94	2.09	-0.25	1.34	0.15	0.89	-0.24	1.73
2000–3000	-0.04	1.33	-1.23	1.85	-0.46	1.29	0.42	0.77	-0.32	1.49
>3000	0.09	1.10	-0.52	1.50	-0.32	1.19	0.33	0.67	-0.09	1.28

one-eighth of China's total landmass, stretching around 1000 km in width from its northernmost to southernmost points and extending up to 2000 km from its eastern to western extremities. It is worth emphasizing that the established model is developed without the incorporation of any station data in Tibet, as depicted in Fig. 1. However, it is remarkable that our model exhibits a commendable capability to produce ZTD with a high degree of accuracy. Despite this absence of station data, our model exhibits an impressive mean RMS difference of 1.55 cm when compared with stations from CMONOC.

However, it is essential to acknowledge that our proposed approach has its limitations. First, this method treats ZTD derived from historical meteorological reanalysis as ground truth values, without accounting for a systematic bias that exists between ERA5-derived ZTD and GNSS-derived ZTD. This inherent bias can hinder the accuracy of our method. It presents a trade-off between meteorology-derived ZTD, which offers global coverage with a higher spatial resolution, and GNSS-derived ZTD, which provides superior accuracy. In future research endeavors, it is imperative to explore avenues to enhance the accuracy of historical gridded ZTD. One promising approach involves amalgamating GNSS-derived ZTD and meteorology-derived ZTD

through a suitable data assimilation technique. The second significant source of error stems from the exponential function applied in the vertical correction. In this study, we used a fixed constant for the exponential function, which simplifies the process but may introduce additional errors when applying the gridded product to the GNSS receiver. To improve accuracy, future work should consider implementing a more precise vertical model, such as a higher-order exponential function (Wang et al. 2022). Additionally, the changing climate is a significant source of errors. As shown in Figs. 7 and 8, the testing results for the year 2022 exhibit larger RMS than the validation sets. This discrepancy arises from the fact that the spatial patterns of ZTD during the period 2012–2021 do not correspond to those observed in 2022. Moreover, in the context of global warming, where water vapor increases with rising temperatures, climate patterns may undergo more substantial changes. While extending the duration for EOF analysis might mitigate the occurrence of highly different patterns, an excessively prolonged analysis period may strain computational resources, exceeding the machine's memory capacity during matrix operations. Finally, it is noteworthy that the temporal resolution of our model is contingent on the time resolution employed in GNSS data analysis.

Conclusions

In this study, we develop a new real-time gridded model with a resolution of $0.25° \times 0.25°$ based on EOF method. We decompose the hourly ERA5-derived ZTD data from 2012 to 2021 into two components: spatial patterns and time series. Subsequently, we employ an ANN to model the time series component, utilizing data collected from 64 stations within the CMONOC network. This new approach capitalizes on both the high spatial resolution of ERA5 and the high accuracy of real-time GNSS-derived ZTD data. To evaluate the efficacy of the proposed model, we conduct validations by comparing its performance with ERA5-derived ZTD and radiosonde-derived ZTD for the year 2022. Additionally, our research involved both internal and external validation to ensure the robustness and reliability of the proposed model. The results show that the EOF-based model can provide a real-time gridded ZTD model with an accuracy of 1.70 cm RMS when compared to ERA5-derived ZTD data for the year 2022. For station-based results, EOFM shows RMS values of 1.86 cm and 2.49 cm when compared to GNSS-derived ZTD data from 234 stations and radiosonde-derived data from 38 stations, respectively. Further discussion explores the mean values for inner and external stations, which demonstrate an RMS of 1.74 cm and 1.89 cm, respectively. The study also investigates the performance of EOFM across different seasons and altitudes. Notably, the real-time model produces relatively accurate ZTD data for the fast-changing water vapor conditions in the south-eastern part of China. These findings underscore the significant accuracy of the proposed model, demonstrating that EOFM achieves accuracy levels comparable to those of other real-time models. Given that the majority of existing real-time models depends on interpolation-based methods, our study seeks to introduce a novel approach specifically designed to provide high precision ZTD estimates in regions with limited or no coverage by GNSS stations.

Author contributions Y.W. and S.J. contributed to the conception of the study and wrote the main manuscript text. S.J. helped review and edit the manuscript. L.C., Z.G., and Y.Z. were responsible for project administration. All authors reviewed the manuscript.

Data availability The ERA5 reanalysis data can be freely downloaded from ECMWF, https://www.ecmwf.int/. The radiosonde data can be downloaded from the University of Wyoming's website, https://weather.uwyo.edu/upperair/sounding.html.

Declarations

Competing interests The authors declare no competing interests.

References

Bevis M, Businger S, Herring TA, Rocken C, Anthes RA, Ware RH (1992) GPS meteorology: Remote sensing of atmospheric water vapor using the global positioning system. J Geophys Research: Atmos 97(D14):15787–15801. https://doi.org/10.1029/92JD01517

Boehm J, Heinkelmann R, Schuh H (2007) Short note: a global model of pressure and temperature for geodetic applications. J Geod 81(10):679–683. https://doi.org/10.1007/s00190-007-0135-3

Böhm J, Möller G, Schindelegger M, Pain G, Weber R (2015) Development of an improved empirical model for slant delays in the Troposphere (GPT2w). GPS Solut 19(3):433–441. https://doi.org/10.1007/s10291-014-0403-7

Chen J, Wu B, Hu X, Li H (2012) SHA: The GNSS Analysis Center at SHAO. In: Sun J, Liu J, Yang Y, Fan S (eds) China Satellite Navigation Conference (CSNC) 2012 Proceedings. Springer, Berlin, Heidelberg, pp 213–221

Chen J, Zhang Y, Zhou X, Pei X, Wang J, Wu B (2014) GNSS clock corrections densification at SHAO: from 5 min to 30 s. Sci China Phys Mech Astron 57(1):166–175. https://doi.org/10.1007/s11433-013-5181-7

Chen J, Wang J, Wang J, Tan W (2019) SHAtrop: empirical ZTD model based on CMONOC GNSS Network. Geomatics Inform Sci Wuhan Univ 44(11):1588–1595. https://doi.org/10.13203/j.whugis20170384

de Oliveira PS, Morel L, Fund F, Legros R, Monico JFG, Durand S, Durand F (2017) Modeling tropospheric wet delays with dense and sparse network configurations for PPP-RTK. GPS Solut 21(1):237–250. https://doi.org/10.1007/s10291-016-0518-0

Ding M (2020) Reducing ZHD–ZWD mutual absorption errors for blind ZTD model users. Acta Geod Geophys 55(1):51–62. https://doi.org/10.1007/s40328-019-00280-6

Guo J, Li X, Li Z, Hu L, Yang G, Zhao C, Fairbairn D, Watson D, Ge M (2018) Multi-GNSS precise point positioning for precision agriculture. Precision Agric 19(5):895–911. https://doi.org/10.1007/s11119-018-9563-8

Hersbach H et al (2023) ERA5 hourly data on pressure levels from 1940 to present. Copernicus Clim Change Service (C3S) Climate Data Store (CDS)

Hinton GE (1989) Learning distributed representations of concepts. In: Morris RGM (ed) Parallel distributed processing: implications for psychology and neurobiology. Clarendon Press/Oxford University, pp 46–61

Jin SG, Luo OF, Ren C (2010) Effects of physical correlations on long-distance GPS positioning and zenith tropospheric delay estimates. Adv Space Res 46(2):190–195. https://doi.org/10.1016/j.asr.2010.01.017

Jin SG, Han L, Cho J (2011) Lower atmospheric anomalies following the 2008 Wenchuan Earthquake observed by GPS measurements. J Atmos Sol -Terr Phys 73(7–8):810–814. https://doi.org/10.1016/j.jastp.2011.01.023

Jin SG, Wang Q, Dardanelli G (2022) A review on Multi-GNSS for Earth Observation and emerging applications. Remote Sens 14(16):3930. https://doi.org/10.3390/rs14163930

Jin SG, Camps A, Jia Y et al (2024) Remote sensing and its applications using GNSS reflected signals: advances and prospects. Satell Navig 5:19. https://doi.org/10.1186/s43020-024-00139-4

Kessler WS (2001) EOF representations of the Madden–Julian Oscillation and its connection with ENSO. J Clim 14(13):3055–3061. https://doi.org/10.1175/1520-0442(2001)014<3055:EROTMJ>2.0.CO;2

Krueger E, Schueler T, Arbesser-Rastburg B (2005) The Standard Tropospheric Correction Model for the European Satellite Navigation System Galileo. Proc. General Assembly URSI, pp, 23–29

Lagler K, Schindelegger M, Böhm J, Krásná H, Nilsson T (2013) GPT2: empirical slant delay model for radio space geodetic techniques. Geophys Res Lett 40(6):1069–1073. https://doi.org/10.1002/grl.50288

Landskron D, Böhm J (2018) VMF3/GPT3: refined discrete and empirical Troposphere mapping functions. J Geod 92(4):349–360. https://doi.org/10.1007/s00190-017-1066-2

Leandro R, Santos M, Langley R (2006) UNB Neutral Atmosphere Models: Development and Performance. 2

Li W, Yuan Y, Ou J, Li H, Li Z (2012) A new global zenith tropospheric delay model IGGtrop for GNSS applications. Chin Sci Bull 57(17):2132–2139. https://doi.org/10.1007/s11434-012-5010-9

Li W, Yuan Y, Ou J, Chai Y, Li Z, Liou Y-A, Wang N (2015) New versions of the BDS/GNSS zenith tropospheric delay model IGGtrop. J Geod 89(1):73–80. https://doi.org/10.1007/s00190-014-0761-5

Li S, Zhou H, Xu J, Wang Z, Li L, Zheng Y (2019) Modeling and analysis of ionosphere TEC over China and adjacent areas based on EOF method. Adv Space Res 64(2):400–414. https://doi.org/10.1016/j.asr.2019.04.018

Li X, Huang J, Li X, Lyu H, Wang B, Xiong Y, Xie W (2021a) Multi-constellation GNSS PPP instantaneous ambiguity resolution with precise atmospheric corrections augmentation. GPS Solut 25(3):107. https://doi.org/10.1007/s10291-021-01123-0

Li X, Wang X, Liao J, Li X, Li S, Lyu H (2021b) Semi-tightly coupled integration of multi-GNSS PPP and S-VINS for precise positioning in GNSS-challenged environments. Satell Navig 2(1):1. https://doi.org/10.1186/s43020-020-00033-9

Lou Y, Huang J, Zhang W, Liang H, Zheng F, Liu J (2018) A New Zenith Tropospheric Delay Grid product for real-time PPP applications over China. Sensors 18(1):65. https://doi.org/10.3390/s18010065

Lu C, Zus F, Ge M, Heinkelmann R, Dick G, Wickert J, Schuh H (2016) Tropospheric delay parameters from numerical weather models for multi-GNSS precise positioning. Atmos Meas Tech 9(12):5965–5973. https://doi.org/10.5194/amt-9-5965-2016

Lu C, Li X, Zus F, Heinkelmann R, Dick G, Ge M, Wickert J, Schuh H (2017) Improving BeiDou real-time precise point positioning with numerical weather models. J Geod 91(9):1019–1029. https://doi.org/10.1007/s00190-017-1005-2

Lu C, Zheng Y, Wu Z, Zhang Y, Wang Q, Wang Z, Liu Y, Zhong Y (2023) TropNet: a deep spatiotemporal neural network for tropospheric delay modeling and forecasting. J Geod 97(4):34. https://doi.org/10.1007/s00190-023-01722-4

Mendes VB, Langley RB (1999) Tropospheric Zenith Delay Prediction Accuracy for High-Precision GPS Positioning and Navigation. Navigation 46(1):25–34. https://doi.org/10.1002/j.2161-4296.1999.tb02393.x

Monahan AH, Fyfe JC, Ambaum MHP, Stephenson DB, North GR (2009) Empirical orthogonal functions: the medium is the message. J Clim 22(24):6501–6514. https://doi.org/10.1175/2009JCLI3062.1

Neha and Pasari S (2022) A review of empirical orthogonal function (EOF) with an emphasis on the co-seismic crustal deformation analysis. Nat Hazards 110(1):29–56. https://doi.org/10.1007/s11069-021-04967-4

Saastamoinen J (1972) Contributions to the theory of atmospheric refraction. Bull Geodesique 105(1):279–298. https://doi.org/10.1007/BF02521844

Schüler T (2014) The TropGrid2 standard tropospheric correction model. GPS Solut 18(1):123–131. https://doi.org/10.1007/s10291-013-0316-x

Sun L, Chen P, Wei E, Li Q (2017) Global model of zenith tropospheric delay proposed based on EOF analysis. Adv Space Res 60(1):187–198. https://doi.org/10.1016/j.asr.2017.03.045

Tsushima H, Hino R, Ohta Y, Iinuma T, Miura S (2014) Geophys Res Lett 41(10):3390–3397. https://doi.org/10.1002/2014GL059863. tFISH/RAPiD: Rapid improvement of near-field tsunami forecasting based on offshore tsunami data by incorporating onshore GNSS data

Wang Y, Jin S (2023) Effect of GNSS radio occultation observations on the prediction of the 2021 Henan rainstorm. GPS Solut 27(3):102. https://doi.org/10.1007/s10291-023-01445-1

Wang J, Balidakis K, Zus F, Chang X, Ge M, Heinkelmann R, Schuh H (2022) Improving the Vertical modeling of Tropospheric Delay. Geophys Res Lett 49(5). https://doi.org/10.1029/2021GL096732. e2021GL096732

White AM, Gardner WP, Borsa AA, Argus DF, Martens HR (2022) A review of GNSS/GPS in Hydrogeodesy: hydrologic loading applications and their implications for Water Resource Research. Water Resour Res 58(7):e2022WR032078. https://doi.org/10.1029/2022WR032078

Xia P, Tong M, Ye S, Qian J, Fangxin H (2023) Establishing a high-precision real-time ZTD model of China with GPS and ERA5 historical data and its application in PPP. GPS Solut 27(1):2. https://doi.org/10.1007/s10291-022-01338-9

Xu X, Tian H, Tian W, Wang Z, Liu H, Qie K, Luo J (2022) The spatiotemporal patterns of the Upper-Tropospheric Water Vapor over the Tibetan Plateau in Summer based on EOF Analysis. J Clim 35(15):5033–5051. https://doi.org/10.1175/JCLI-D-21-0720.1

Xu C, Liu C, Yao Y, Wang Q, Wang X (2023) Tibetan zenith wet delay model with refined vertical correction. J Geod 97(4):31. https://doi.org/10.1007/s00190-023-01719-z

Yang F, Guo J, Li J, Zhang C, Chen M (2021) Earth Space Sci 8(8):e2021EA001815. https://doi.org/10.1029/2021EA001815. Assessment of the Troposphere Products Derived From VMF Data Server With ERA5 and IGS Data Over China

Yao Y, Xu C, Shi J, Cao N, Zhang B, Yang J (2015) ITG: a New Global GNSS Tropospheric correction model. Sci Rep 5(1):10273. https://doi.org/10.1038/srep10273

Zhang H, Yuan Y, Li W, Zhang B, Ou J (2018) A grid-based tropospheric product for China using a GNSS network. J Geod 92(7):765–777. https://doi.org/10.1007/s00190-017-1093-z

Zhang H, Yuan Y, Li W (2022) Real-time wide-area precise tropospheric corrections (WAPTCs) jointly using GNSS and NWP forecasts for China. J Geod 96(6):44. https://doi.org/10.1007/s00190-022-01630-z

Zhang D, Chen L, Yuan Y, Zuo J, Ke Z (2023) Why was the heat wave in the Yangtze River valley abnormally intensified in late summer 2022? Environ Res Lett 18(3):034014. https://doi.org/10.1088/1748-9326/acba30

Yu Wang   is a Ph.D student at Shanghai Astronomical Observatory, Chinese Academy of Sciences, Shanghai, China. He received his B.Sc degree from Nanjing University of Information Science and Technology in 2022. His current research mainly focuses on GNSS meteorology, tropospheric modelling and climate dynamics.

Shuanggen Jin   is a Professor at Shanghai Astronomical Observatory, Chinese Academy of Sciences, China, Vice-President & Professor at Henan Polytechnic University, China, and a Member of Academia Europaea, Member of the European Academy of Science and Member of the Turkish Academy of Sciences. He received a B.Sc in Geodesy from Wuhan University, China in 1999 and a Ph.D in Geodesy from the University of Chinese Academy of Sciences in 2003. He has been on Satellite Navigation, Space Geodesy, Remote Sensing, and Space/Planetary Exploration with over 500 peer-reviewed papers and more than 15,000 citations.

Cheng Liu   is a Senior Engineer and Director at the Institute of Surveying, Mapping, and Geographic Information of China Railway Design Corporation. He is an expert at China State Railway Group Co., Ltd, as well as a registered surveyor and registered safety engineer. He has been involved in technical research and practical production related to high-speed railway precision engineering controlling, railway satellite positioning, airborne LiDAR, digital photogrammetry, and other railway engineering surveying techniques.

Guanjun Zhang   is a Senior Engineer and Chief Engineer at the Institute of Surveying, Mapping, and Geographic Information of China Railway Design Corporation. He serves as Deputy Director of the Tianjin Key Laboratory of Rail Transit Navigation, Positioning, and Spatial-temporal Big Data Technology. He is Vice Chairman of the Engineering Survey Branch of the Chinese Society for Geodesy Photogrammetry and Cartography, Member of the Chinese National Surveying and Mapping Geographic Information Measurement and Testing Technical Committee and Member of the Railway Beidou Special Committee of GNSS & LBS Association of China. He received a Master's degree in Surveying and Mapping Engineering from Wuhan University, Wuhan, China. His primary interests include precise engineering surveying, satellite positioning, railway engineering deformation monitoring, and international engineering surveying.

Yunlong Zhang   is a Senior Engineer at the China Railway Design Corporation in Tianjin, China. He received his Ph.D. from Beijing Jiaotong University, Beijing, China. His research primarily focuses on Beidou + Seamless PNT, Beidou surveying, and Beidou deformation monitoring and detection.